

# 3D Segmentation of the Mouse Spleen in microCT via Active Contours

Deniz Aykac, Jeffery R. Price, Jonathan S. Wall

**Abstract**— We present in this paper a novel method for 3D segmentation of the mouse spleen in x-ray CT (microCT) data. Our approach is based upon the 2D “active contours for smooth without edges” algorithm. We introduce a simple statistical weighting scheme that improves region contrast and segmentation performance. We extend the 2D approach to 3D by slice-to-slice processing, including the 3D flow of image statistics. The technique requires no training and operates semi-automatically, requiring only the entry of a single seed point within the spleen. Results are shown that demonstrate the effectiveness of our approach.

**Index Terms**—Level sets, active contours, 3D segmentation, microCT, spleen.

## I. INTRODUCTION

THE proliferation of small animal imaging technologies has enabled high-resolution studies of biological mechanisms and structures in mouse models. Such technology allows researchers to perform longitudinal studies on animals to monitor disease progression and regression *in vivo*. The work we present herein is motivated by high-resolution, dual-modality SPECT/CT imaging to quantify amyloid deposits in the spleen of a transgenic mouse model of AA-amyloidosis [1]. The goal of our work is to volumetrically segment the spleen in contrast-enhanced microCT data. The spleen segmentation will subsequently be used to build an attenuation map for microSPECT correction [2] and to quantify the amount of radiotracer accumulated in the corresponding volume of the functional SPECT data.

There has been much research in recent years aimed at the segmentation of biological images. Active contours or deformable models are perhaps the most successful class of techniques used for segmentation. Within the larger class of deformable models, active shape models (ASM) or active appearance models (AAM) [3] are well-suited for applications where *a priori* information is available for incorporation into the segmentation process. These model-driven methods suffer from practical limitations in the training process, especially 3D. The user must consistently label a set of landmark points, with correct correspondence on the surface of every 3D structure in the training set. Another successful deformable model approach is the level-set formalism where a closed curve representing the structure of interest iteratively

propagates towards the desired boundary through the evolution of an implicit function [4], [5]. In most of the level-set approaches, the curve evolves based on the image gradient. Hence, only objects with well-defined edges can be found.

There are three problems that arise related to spleen segmentation with respect to the above-mentioned techniques. First, the spleen shape and size varies widely between animals; which limits the use of *a priori* correspondence and training. Second, even with the use of a contrast agent, the image intensity values within the spleen are very non-homogenous (due to the follicular architecture in the spleen, see Fig. 1), leading to discontinuous boundaries. Finally – and again even with the use of a contrast agent – the spleen has smooth edges. With these problems in mind, we adopt and modify a recently developed active contour model [6] that is more suitable for objects with smooth edges.

We begin with the 2D level-set active contour model proposed by Chan and Vese [6]. We introduce an image weighting term, based on local statistics, to enhance the spleen region. Although the level-set method can be explicitly implemented in 3D, we extend the original 2D method to 3D via a 2D slice-by-slice approach, but with a 3D flow of local statistical information. This approach allows the method to adapt, from slice-to-slice, to the changing statistics that we have observed in our data. In Section II below, we briefly summarize our approach and in Section III we present experimental results.

## II. METHOD

The 2D active contour model [6] with which we begin can be seen as an energy minimization problem and formulated in terms of level-set functions. The basic idea behind the method is to create an energy term that is minimized when the initial curve reaches the desired boundary. We start with the assumption, as in Chan’s model, that the image,  $I_0$ , is formed by two approximately homogenous regions, one corresponding to the object of interest and the other to the background. The average intensities inside and outside the object are  $c_1$  and  $c_2$ , respectively, and the evolving curve  $C$  is defined as the boundary of the object. Since we desire a smooth boundary, we also employ a regularizing term based on the length of the curve  $C$ . The resulting energy term we seek to minimize can then be written as:

D. Aykac is with the Oak Ridge National Laboratory, Oak Ridge, TN 37831 USA (telephone: 865-576-2004, e-mail:aykacdb@ornl.gov).

J. R. Price is with the Oak Ridge National Laboratory, Oak Ridge, TN 37831 USA (telephone: 865-574-5743, e-mail:pricejr@ornl.gov).

J. S. Wall is with the University of Tennessee Graduate School of Medicine, Knoxville, TN 37920 USA (telephone: 865-544-9165, e-mail:jwall@mc.utmc.edu).

$$E(c_1, c_2, C) = \mu \cdot \text{Length}(C) + \int_{\text{inside}(C)} |I_o(x, y) - c_1|^2 dx dy + \int_{\text{outside}(C)} |I_o(x, y) - c_2|^2 dx dy. \quad (1)$$

The balance between the homogeneity (last two terms) and smoothness (first term) is controlled by the single parameter  $\mu$ . We minimize the above energy term using a level-set approach where the curve  $C$  is represented as the zero level set of a Lipschitz function  $\phi$ :

$$\begin{aligned} C &\Rightarrow \phi(x, y) = 0 \\ \text{length}(C) &\Rightarrow \partial \omega \\ \text{inside}(C) &\Rightarrow \omega, \phi(x, y) > 0 \\ \text{outside}(C) &\Rightarrow \Omega \setminus \omega, \phi(x, y) < 0 \end{aligned} \quad (2)$$

Following the Euler-Lagrange construction in [6], the level-set curve evolution can be written:

$$\frac{\partial \phi}{\partial t} = \delta_{\mathcal{E}}(\phi) \left[ \mu \cdot \text{div} \left( \frac{\nabla \phi}{|\nabla \phi|} \right) - (I_o - c_1)^2 + (I_o - c_2)^2 \right] = 0, \quad (3)$$

where  $t$  is an artificial time variable that parameterizes the descent iteration, and  $H_{\mathcal{E}}(\phi(x, y))$  and  $\delta_{\mathcal{E}}(\phi(x, y))$  are regularized Heaviside and Dirac functions, respectively, given by:

$$\begin{aligned} H_{\mathcal{E}}(z) &= \frac{1}{2} \left( 1 + \left( \frac{z}{\varepsilon} \right) \arctan \left( \frac{z}{\varepsilon} \right) \right) \\ \delta_{\mathcal{E}}(z) &= H'_{\mathcal{E}}(z) = \frac{1}{\pi} \frac{\varepsilon}{\varepsilon^2 + z^2} \end{aligned} \quad (4)$$

We numerically approximate the iteration of (3) using the same finite difference scheme as described in [6] and based upon earlier work in [8]:

$$\begin{aligned} \phi_{i,j}^{n+1} &= \phi_{i,j}^n + \Delta t \cdot \delta_h(\phi_{i,j}^n) \cdot \left[ \frac{\mu}{h^2} \Delta_x^- \left( \frac{\Delta_+^x \phi_{i,j}^n}{\sqrt{(\Delta_+^x \phi_{i,j}^n)^2 / h^2 + (\phi_{i,j+1}^n - \phi_{i,j-1}^n)^2 / (2h)^2}} \right) \right. \\ &+ \frac{\mu}{h^2} \Delta_y^- \left( \frac{\Delta_+^y \phi_{i,j}^n}{\sqrt{(\Delta_+^y \phi_{i,j}^n)^2 / h^2 + (\phi_{i+1,j}^n - \phi_{i-1,j}^n)^2 / (2h)^2}} \right) \\ &\left. - (I_{o,i,j} - c_1 (\phi_{i,j}^n))^2 + (I_{o,i,j} - c_2 (\phi_{i,j}^n))^2 \right] \end{aligned} \quad (5)$$

where  $h$  is the space step,  $\Delta t$  is the time step,  $\phi_{i,j}^{n+1} = \phi(n\Delta t, x_i, y_j)$ , and the finite differences are given by

$$\begin{aligned} \Delta_x^- \phi_{i,j} &= \phi_{i,j} - \phi_{i-1,j}; \quad \Delta_x^+ \phi_{i,j} = \phi_{i+1,j} - \phi_{i,j} \\ \Delta_y^- \phi_{i,j} &= \phi_{i,j} - \phi_{i,j-1}; \quad \Delta_y^+ \phi_{i,j} = \phi_{i,j+1} - \phi_{i,j} \end{aligned} \quad (6)$$

The initial  $\phi_{i,j}^0$  is set to be the signed distance function to the initial curve, where the points inside the zero level-set are positive and those outside are negative. At the end of the above iterative process, determined by essentially no change between successive iterations, the zero level-set of  $\phi_{i,j}^n$  defines the border of the object of interest.

The main assumption in Chan's method, as described above, is that image is formed by two approximately homogenous regions of constant intensities  $c_1$  and  $c_2$ . We note, however, that the interior of the spleen is not homogenous, as can be seen Fig. 1(a), where dark regions correspond to follicles and brighter regions to blood (with contrast agent). Also evident in these figures is the subtleness of the spleen boundary, which is exacerbated by follicles that appear near the border in some slices. To solve these issues, we adopt the following approach.

We begin with a single seed point  $(x, y, z)$  coordinates near the center of the spleen that has been manually selected by the biologist reviewing the reconstructed images. We set the initial boundary to a small circle around this seed point in the given slice and compute local statistics (mean  $\mu$  and standard deviation  $\sigma$ ) of the intensity values within this boundary. We compute a statistical weighting image,  $W_s(x, y)$ , where each pixel is set proportional to the value of the normal distribution defined by  $\mu$ ,  $\sigma$ , and the corresponding intensity value in the original image:

$$W_s(x, y) = \exp \left( \frac{-(I_o(x, y) - \mu)^2}{2\sigma^2} \right) \quad (7)$$

Next, a proximity weighting image,  $W_p(x, y)$ , is computed where the values are set to the inverse of the distance from the given grid point  $(x, y)$  to the closest point on the initial boundary  $(x_c, y_c)$ :

$$W_p(x, y) = \frac{1}{\sqrt{(x - x_c)^2 + (y - y_c)^2}}. \quad (8)$$

For a given slice, we then apply the level-set algorithm described above to the product of the original intensity image and these two weighting terms. An example showing the original intensity image and the weighted images can be seen in Fig. 1. Since the level-set method allows topological changes, multiple contours are often found, including follicles within the spleen and/or high-contrast structures outside the spleen. To alleviate this problem, we simply keep the longest contour that encloses the seed point. We do note, however,

that segmentation of the follicles within the spleen can in fact be desirable and will be important in our ongoing work.

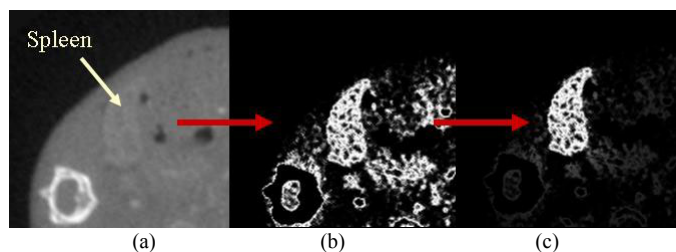


Fig. 1: (a) Original gray-scale image,  $I_0(x, y)$ . (b) Statistically weighted image,  $I_0(x, y) \times W_s(x, y)$ . (c) Result of statistical and proximity weighting,  $I_0(x, y) \times W_s(x, y) \times W_p(x, y)$ .

To achieve 3D segmentation, we proceed from the initial (approximately central) slice in both  $z$  directions in a slice-by-slice fashion. The statistical and proximity weighting images for each successive slice are computed using the final boundary from the preceding slice. This allows us the gray-scale statistics to adapt to changing intensity distributions, which is important since the organ of interest may exhibit such changes due to varying uptake of the contrast agent. When multiple contours are found (i.e., follicles, nearby bones, etc.) after convergence, the longest contour that contains the centroid of the boundary from the preceding slice is kept. This procedure is repeated through the entire volume until the extracted boundaries are suitably small (i.e., approximately less than 10 pixels). The 3D spleen surface then comprises the collection of all contours from the 2D slices.

### III. RESULTS

We have tested our approach on four mouse (Balb/C wild type) data sets comprising 768 slices of  $512 \times 512$  pixels each with a slice thickness of 0.1mm. CT reconstruction was performed using a fast Feldkamp method [7]. The spleen was enhanced with  $350 \mu\text{l}$  of vascular contrast agent Fenestra VC (Alerion Biomedical Inc, San Diego, CA), which was intravenously administered through the tail vein.

We have compared our method to manual segmentation results in these four data sets. The manually segmented data comprises one entire spleen (all slices) and 10 randomly selected slices from each of the other three data sets. We refer to the complete data set as BalbVC1. Surface rendering of manually and automatically segmented spleens for BalbVC1 is shown in Fig. 2 (constructed using Amira visualization software)

Manual segmentation was performed by an expert in mouse studies and implemented in the Amira software environment by cropping to the minimal volume containing the spleen and using slice-by-slice thresholding. For BalbVC1, the manual segmentation took about two hours (with constant user interaction). Two slices from BalbVC1 data set are shown in Fig. 3. We can see that the manual result fails to capture

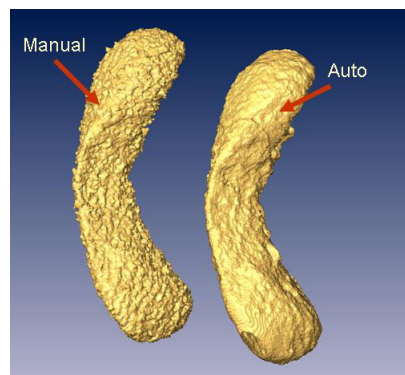


Fig. 2: Surface rendering of manually and automatically segmented spleens from BalbVC1 data set.

some parts of the spleen, missing follicles that are near the boundary. The best and the worst matches between our result and the manual segmentation results are determined based on the RMS distance between points on our boundary and the corresponding nearest points on the manually segmented boundary as shown in Fig. 4. In our result, part of a nearby blood vessel, with nearly identical mean gray value to the spleen, was captured by our algorithm in an earlier slice. This propagated to a few subsequent slices (e.g., 523) as seen in Fig. 4. We are developing a method to address such problems in ongoing work.

As described previously, the statistical and proximity weighting images for each successive slice are computed using the final boundary from the preceding slice. This allows us to adapt to changing intensity distributions. This is important since the organ of interest may exhibit such changes due to varying uptake of the contrast agent. Fig. 5 shows how the mean gray value and standard deviation inside the spleen change through the slices.

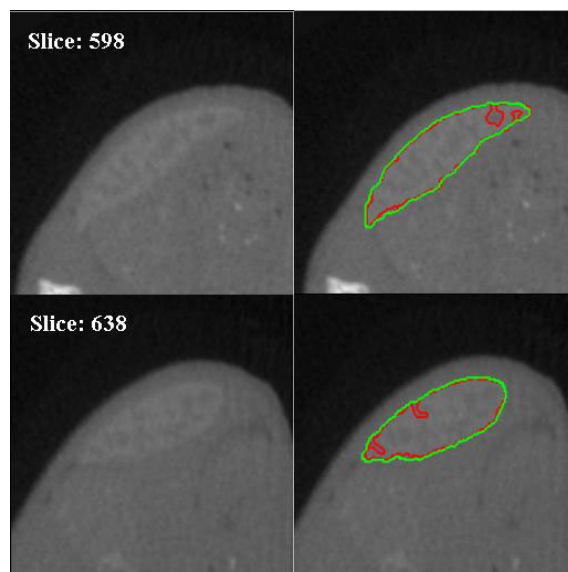


Fig. 3: Examples from the BalbVC1 data set. The original images are shown on the left and the segmentation results on the right. Note the lack of a sharp gradient at the spleen boundary and the subtle contrast difference between the spleen and other regions. Our result is given by the green boundary and the manual segmentation is the given by red boundary.

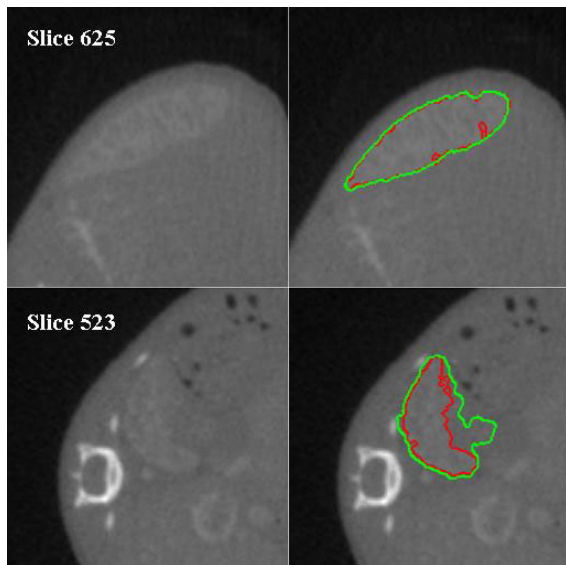


Fig. 4: The original images from BalbVC1 are shown on the left and the segmentation results on the right. Slice 625 represents the closest match. The result for slice 523 represents the worst match between our result and the manual result.

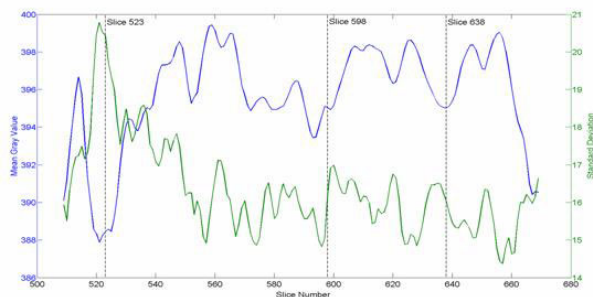


Fig. 5: This plot shows the mean (blue) and standard deviation (green) inside the spleen vs. slice number.

We note that our results from the other three data sets (of with 10 manually segmented slices each) were actually better than those shown above for BalbVC1. The closest match between our results and manual results over all of the experimental data is shown in Fig. 6. For the other data, our result and the manual result were either nearly identical or our result captured the true boundary while the manual result missed near-boundary follicles.

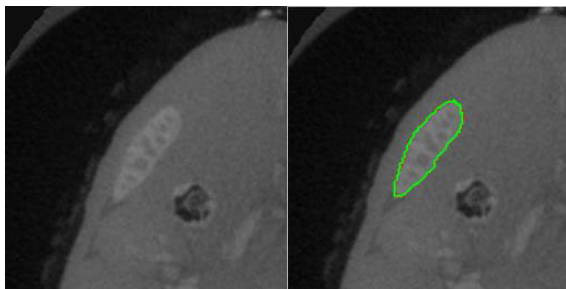


Fig. 6: Left the original image, Right our results and the manual results overlaid on original image (the red and green boundaries essentially overlap).

#### IV. CONCLUSION AND FUTURE WORK

We have implemented a 3D segmentation method based on the 2D “active contours without edges” approach. The statistical weighting scheme and proximity relation were added to solve a challenging segmentation problem. We extended the original 2D method to 3D via a slice-by-slice approach, but with a 3D flow of local statistical information. This approach allows the method to adapt, from slice-to-slice, to the changing statistics that we have observed in our data. In the future, we will employ the topology changing feature of the level set approach to also segment follicles within the spleen. The segmentation of these follicles is important since the result will provide information on the true blood volume to and will thereby facilitate the quantification of amyloid deposits. We can segment these follicles by initializing to our segmented boundary and then using level sets to detect only structures inside the spleen. A preliminary result on one slice is shown in Fig. 7.

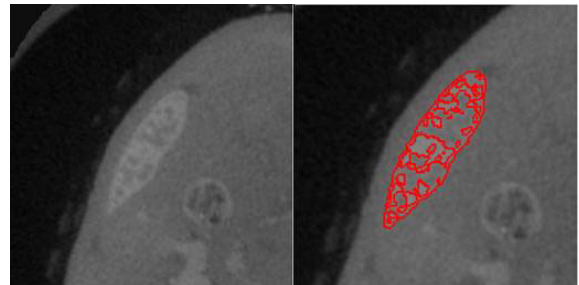


Fig. 7: Left, original image, Right, segmented follicles overlaid on original image.

#### V. REFERENCES

- [1] J.S.Wall, S.J.Kennel, M.J.Paulus, S.Gleason, J.Gregor, J.Baba, M.Schell, T.Richey, B.O’Nuallain, R. Donnell, P.N.Hawkins, D.T.Weiss, A.Solomon, “Quantitative high-resolution microradiographic imaging of amyloid deposits in a novel murine model of AA-amyloidosis”, *Amyloid: The J. of Protein Folding Disorders*, in press.
- [2] N. Black, J. Gregor “Monte Carlo study of attenuation and scatter for microSPECT.” Sub. to the IEEE Nuc Sci. Symp. Med. Imag. Conf., 2005.
- [3] T.F.Cootes,G. J. Edwards,C. J. Taylor “Active appearance models”, *IEEE Trans. On Pattern Analysis and Machine Intelligence*, vol.23, No.6: 681-685, 2003.
- [4] R.Malladi, J.Sethian, B.Vemuri “Shape modeling with front propagation: a level set approach”, *IEEE Trans. On Patt. Anal. and Mach Intell*, vol.17, No.2: 158-175, 1995.
- [5] C. Baillard, P. Hellier, C. Barillot “Segmentation of 3D brain structures using level sets and dense registration,” in *Proc. Of the IEEE Workshop on Math. Meth in Biomedical Image Analysis*, pp. 94-101, 2000.
- [6] T. F. Chan, L. A. Vese “Active contours without edges,” *IEEE Trans. on Image Processing*, vol.10, No.2: 266-277, 2001.
- [7] J. Gregor, S. Gleason, M. Paulus, J. Cates “Fast Feldkamp reconstruction based on focus of attention and distributed computing,” *Intl. J. for Imaging Systems and Technology*, v. 12, pp. 229-234, 2002.
- [8] G. Aubert, L. Vese, “A variational method in image recovery”, *SIAM: J. Num. Anal.*, 34/5, 1948-1979, 1997.